Solar Dish Concentrator: A Case Study at the Energy Center Rooftop

Hindawi
International Journal of Energy Research
Volume 2023, Article ID 9658091, 18 pages
https://doi.org/10.1155/2023/9658091

Research Article

Solar Dish Concentrator: A Case Study at the Energy Center Rooftop

Antonio Marra,[1] Massimo Santarelli,[1] and Davide Papurello[1,2]

[1]*Department of Energy (DENERG), Politecnico di Torino, Corso Duca degli Abruzzi, 24, 10129 Turin, Italy*
[2]*Energy Center, Politecnico di Torino, Via P. Borsellino 38-16, 10138 Turin, Italy*

Correspondence should be addressed to Davide Papurello; davide.papurello@polito.it

Received 23 January 2023; Revised 20 July 2023; Accepted 29 July 2023; Published 10 August 2023

Academic Editor: Gianluca Coccia

Concentrating solar technology plays a role, albeit a niche role compared to commercial solar systems (photovoltaics and thermal collectors). Within the context of sustainable development and within the green transition phase, it could be a respectable player. The main purpose of this study is to create and validate a model that approximates the temperature trend of a receiver installed in a CSP (concentrated solar plant). A method to approximate optical and thermal performance is discussed. The paraboloid installed in the Energy Center (Turin, Italy) was taken as a reference, creating a model that could simulate real operating conditions. The Monte Carlo (MC) method for ray tracing was adopted developing two models. The first model sets the maximum reflectivity of the paraboloid and neglects the loss of "limb darkening," while the second one sets a reflectivity of 80%. Once the incident flux was obtained, the optical performance was analytically calculated and compared to the value provided by the manufacturer. The thermal performance was also studied, reproducing the dimensions of the receiver consisting of a sintered alumina tube placed at a focal distance from the paraboloid. Two configurations were analyzed: one neglecting the losses due to radiation and natural convection, the other one including the losses due to radiation and considering the atmospheric wind condition. Finally, the model was validated by comparing the obtained temperatures with those measured by thermocouples placed on the receiver. Analyzing two random days in the year 2020, an average error of 7% and 2% was obtained.

1. Introduction

Global warming, overpopulation, and the increase in energy demand have led to the need of finding alternative sources for energy production. The abandonment of fossil fuels places attention on the study of clean and nonexhaustible energies. Solar energy can be considered the most promising renewable source because it is regenerative, clean, and sustainable [1]. Photovoltaic plants (PV) and CSP are the best-known technologies to convert solar energy [2–7]. There are also other studies focusing on PV-TE (Photovoltaic-thermoelectric) systems capable of transforming the superfluous part of solar heat, keeping the panel at an almost constant temperature [5, 6, 8]. CSP and PV systems produce electric energy from the solar source and involve the installation of a thermal energy storage (TES) system [9] which makes energy production independent from solar radiation [10] and therefore for use at night or during times when there is no sunlight. The following flow chart shows the general operations of a CSP plant (see Figure 1).

Among the various CSP technologies, the most important can be distinguished by the following:

(i) *Solar Power Tower (SPT)*. The reflector is formed by a series of mirrors (heliostats) equipped with a double-axis tracking system that converges the rays on a receiver placed on a tower. The materials for the receiver are generally ceramics or metals, which are stable at elevated temperatures [12]. These plants have a range of average solar flux from 200 kW/m^2 to 1000 kW/m^2 [13], and they can have an electrical power of 100 MW [14]

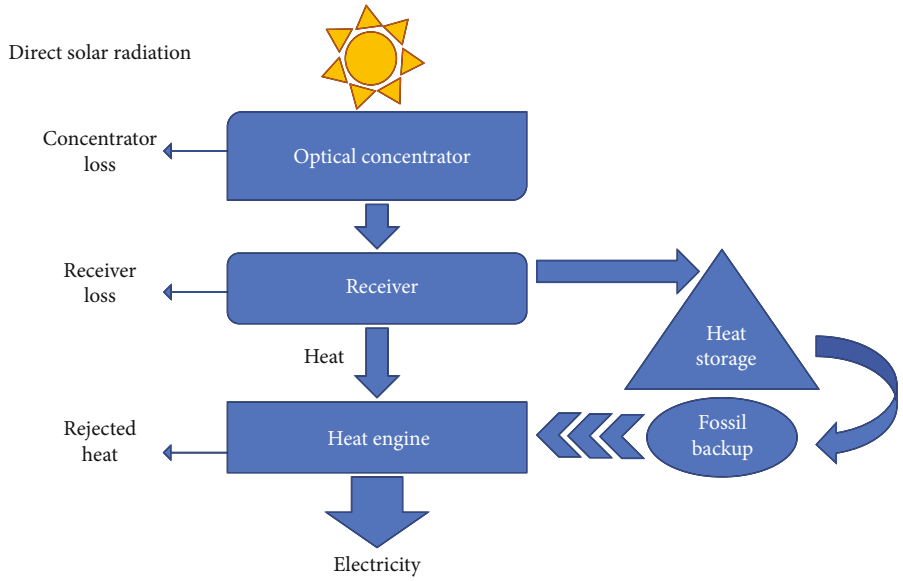

Figure 1: Scheme of the main parts of a solar dish system with storage, including possible losses [11].

(ii) *Parabolic Trough Collector (PTC)*. The rays are concentrated on a focal line where a cylindrical horizontal receiver is positioned. The temperature of the working fluid can reach 400°C [15] and the electrical efficiency of around 15% [16]. The turbine's net mechanical power varies between 25 MW and 50 MW, but plants can have a capacity of 1 MW [12]

(iii) *Linear Fresnel Reflector (LFR)*. The concentrator is made up of flat or slightly curved mirror segments. The receiver tube, positioned along the focal axis, is fixed, and handling only concerns the concentrator [17]. The capacities are between 10 and 200 MW, with a range of electrical efficiency of about 8-10% [18]

(iv) *Solar Parabolic Dish (SPD)*. It is a parabolic point-focus concentrator. A dish that reflects solar radiation into a receiver's focal point. The capacity ranges from 0.01 to 0.5 MW, and they are generally accompanied by a Stirling cycle with an electrical efficiency between 25% and 30% [6, 12]

The SPD system, thanks to the high temperature reached by the working fluid [19, 20], can use several types of cycles. Options studied include organic Rankine cycle turbines with toluene [21, 22], Stirling engines with hydrogen or helium [23, 24], open and closed-air Brayton cycles, and also power cycles suitable for small power stations [25], such as Rankine cycle engines with steam [26]. Numerous studies are trying to find an appropriate model that describes the solar concentrator. The model validation will make it possible to choose the best cycle in terms of achievable operating ranges. Finite element method (FEM) software is used to estimate the performance of the CSP. It is also necessary to carry out a MC simulation to evaluate the optical efficiency. Fritsch et al. studied the thermal behavior of a tube-type receiver flowed by molten salts making a comparison between computational fluid dynamics (CFD) and FEM. The results show good agreement between the two approaches. The simplified model with one-dimensional fluid elements and a constant heat transfer coefficient is therefore valid for this purpose [27]. Fang et al. analyzed thermal characteristics and thermal stress in a steam/superheat solar cavity finding a CFD model, which couples the thermal analysis and the thermoelastic analysis. Thanks to this study, the causes of thermal stress induced by different temperature gradients on the absorber tubes have been identified [28]. Pierucci et al. designed a prototype of a collector for residential applications that could also be used to feed a bottoming small-scale organic Rankine cycle (ORC) system for cogeneration or an absorption chiller for air cooling purposes. Through optical analysis, they optimize mirror parameters (rim angle and aperture of the parabola, optical errors, etc.). Then, the results have been used as the boundary conditions for the numerical model of the receiver, and, finally, a 3D FEM model to have a prediction of the thermal performance [29]. Gilioli et al. propose a methodological approach that combines experimental testing and modelling technique to design an LFR collector. They focused on a structural investigation to reproduce the global behavior of the collector (displacement, rotation, and stiffness) [30].

This paper aims to build a model that approximates the temperature performance of the small solar dish located on the roof of the Energy Center (Turin, Italy). The goal is to find a simple and general method that, using FEM simulations, can approximate the optical and thermal performance of a receiver installed in an SPD system. Two fundamental objectives have been identified in this research work.

(i) Starting from a real reflector case, a method is realized that can approximate the optical performance in the face of an ideal and real case with MC ray-tracing simulation

(ii) To realize a method that exploits thermophysical properties to achieve the thermal performance of the CSP receiver

The optical and thermal boundary conditions can be used as input for a generic power cycle (Stirling, Brayton, or Rankine cycle). Concentrator performance can be evaluated to find the most suitable power conversion cycle. In fact, these data will be used as input to power a small organic Rankine cycle (ORC).

2. Material and Methods

The main points of modelling an SPD system are investigated and reported. The reflector placed on the Energy Center roof will be taken as a reference, and the temperatures obtained by the model will be compared with those recorded by the thermocouples placed on the receiver. COMSOL Multiphysics (Comsol Inc., Sweden (https://www.comsol.com/)) was adopted for the modelling study. The optical and thermal modules will be used. A first model will estimate the optical properties of the reflector-receiver system using a MC ray-tracing simulation ("Monte Carlo ray tracing method"). The generation of solar rays occurs through a purely random phenomenon to estimate physical characteristics, such as reflector surface roughness, and geometric characteristics, the irradiated surface of the receiver with a probabilistic distribution [31]. A second simulation will be dedicated to the analysis of thermal dispersion losses in the absorber.

2.1. CSP Description. The concentration system has a disc reflector, which converges the sun's rays on a tubular receiver placed at a focal distance. The aluminium paraboloid is coated with a polymer layer, which provides high reflectivity and good optical properties (Elma net Srl, Italy, https://www.elmanet.info/). The receiver is made of an alumina (Al_2O_3) tube able to withstand high temperatures (Almath Crucibles Ltd., UK, https://almathcrucibles.com/).

The reflector surface has a remarkable efficiency; with normal direct irradiation (G) of 800 W/m^2, it reaches an optical efficiency (η_{ott}) of 80% and can produce a thermal power (Q_c) equal to 2.8 kW, while temperatures above 1800°C can be reached at the focal point [32]. The direct solar irradiance values were recorded with the STR-21G Sun tracker (Eko Instruments, Den Haag, Netherlands, https://www.eko-instruments.com/eu). In Figure 2, in the lower part of the disc, the movable support of the solar tracking system is shown, which allows optimal exposure to solar radiation [26]. In the following table, the reflector data for the CSP are presented. The focal length (f) and the rim angle (Φ_{rim}) are the most important parameters to determine the reflector diameter and the capturing area of the concentrator (see Table 1). The focal length is the distance from the vertex to the focus point, while the rim angle is the angle between the axis and a line from the focus to the physical edge of the concentrator. The above parameters completely define the cross-sectional geometry.

The receiver has been sized considering a cylindrical geometry placed horizontally. The cylinder size has been obtained by taking as reference the dimensions of the real focal plane (see Figure 3).

The total length was obtained by taking points T1 and T3 as extremes (3.7 and 20.7 cm); the diameter of the receiver is 18 mm. T1, T2, and T3 represent the positioning points of the K-type thermocouples that record the temperature trend in the focal plane (see Figure 3). The N-type thermocouples (Tersid Srl, Italy, https://www.tersid.it/) are composed of nicrosil/nisil and they have a high working range from -270°C to 1300°C. An internal thermocouple (T0) type B (Tersid Srl, Italy, https://www.tersid.it/) was installed inside the cylinder (same point of T2), consisting of platinum and rhodium which allows the recording of temperatures above 1800°C [33]. The latter will be crucial in the validation phase of the experimental model (see Figure 4).

3. Results

3.1. Optical Model. The geometry of the reflector and receiver was implemented in the model (see Table 1). The mesh choice is crucial to achieving accurate results. The choice fell on the densest possible discretization configuration, selecting the "extremely fine" configuration from COMSOL (see Figure 5). There are two views of the same testing setup: top view (a) and side view (b). In Figure 5(a), it is possible to see the x-axis centered on the focal point and receiver, and it is also visible the depth of the solar disc. In Figure 5(b), the mesh selection of the entire solar disc is visible.

In the following figure (Figure 6), the receiver mesh was reported, also in this case, the selected mesh is "extremely fine."

In the simulation, 10^5 solar rays (n_{rays}) are emitted which hit the reflector; their direction depends on the vector of the arrival ray and the surface normal, while their intensity depends on the power of the source. The irradiance reflected on the receiver depends on the geometric and reflection characteristics of the reflector. The cases of the ideal and real reflector are now analyzed.

3.1.1. Ideal Case versus Real Case. The incident irradiance on the receiver varies according to the geometric and reflection characteristics of the reflector. The direct normal irradiation (G) is set to 800 W/m^2, while the maximum opening angle of the disc is $\theta_s = 4.65$ mrad. Diffuse and reflected radiations are not exploited by the solar concentrator. In the ideal case, the paraboloid is perfectly smooth and reflective, neglecting absorption losses. Instead, the real case considers "the limb darkening" phenomenon which will cause a decrease in the performance of the reflector (see Figure 7). This leads to a reduction in the intensity of solar radiation that affects the receiver. In agreement with the manufacturer [32], the absorption coefficient of the reflector α_r is set equal to 0.2 which means that only 80% of the radiation will be concentrated (see Table 2).

It is important to focus on the solar radiation deposited by the reflector on the receiver, which has a higher radiation in the central zone and tends to gradually decrease as it approaches the edges of the dish. The receiver, placed at a focal distance, can capture the radiation reflected by the paraboloid. In the ideal case, the concentration of the rays by the reflector takes place precisely, without any dispersion (see Figure 7(a)). Here, the trajectory of the rays is uniform

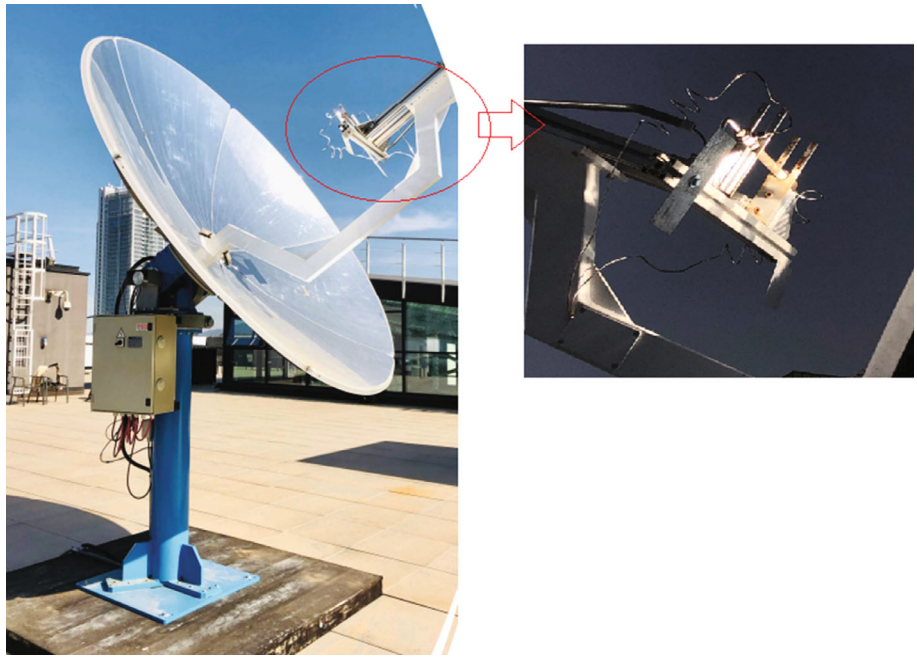

Figure 2: Solar dish concentrator at the Energy Center.

Table 1: Reflector data for the CSP.

Name	Expression	Value	Description
f	0.92	0.92 m	Focal length
Φ_{rim}	45°	0.7854 rad	Rim angle
D_C	$4 \cdot f \cdot (\csc(\phi_{\text{rim}}) - \cot(\phi_{\text{rim}}))$	1.80 m	Reflector diameter of the concentrator
A_C	$\pi \cdot d^2/4$	2.54 m^2	Capturing the area of the concentrator

and ranges from 3.95 to $4.2 \cdot 10^{-2}$. In the real case, the direction of the rays striking the receiver deviates due to the surface roughness of the paraboloid (see Figure 7(b)). Here, the number of rays that reach the receiver is smaller and wider (3.4 to $40 \cdot 10^{-3}$). Therefore, all the rays are unable to reach the focal area of the receiver, causing an incident loss of flux. The power absorbed by the receiver is then estimated. Once the "Wall" condition has been set in COMSOL, it is possible to estimate the incident flux on the receiver (Φ_{ave}). The deposited thermal flux is reported in Figure 8.

As can be seen in the ideal case (Figure 8(a)), the distribution of the incident flux is almost circular, has higher values near the focal point, and gradually decreases. The maximum flow rate recorded is approximately $2.02 \cdot 10^7$ W/m^2. A plausible estimation of uncertainty in the model indicates a maximum value variability of around 10%. In the real case (Figure 8(b)), it shows a net decrease in the maximum flow caused by the losses mentioned above. The maximum value of the incident flux is $1.11 \cdot 10^7$ W/m^2, and the focal area is wider than in the ideal case due to the deviation of the sun's rays. Here, the variability estimation is more difficult than in the ideal case. The model is also able to derive the temperature trend and therefore to trace the maximum temperature reached on the surface of the receiver (see Figure 9).

For the ideal case (Figure 9(a)), the maximum temperature (T_{max}) is 4344 K, reached at the single point, with a heat flux of $2.02 \cdot 10^7$ W/m^2 (Φ_{max}). This is a very high value, related to the assumed ideal conditions of perfect paraboloid reflection. The imperfect convergence of the rays in the real case (Figure 9(b)) induces an elliptical distribution also for the temperature, recording a maximum temperature lower than the ideal case and equal to 3739 K (T_{max}) (see Table 3).

The optical properties of the real case are assessed by comparing the results obtained from the model with the data provided by the manufacturer (Elma net Srl, Italy, https://www.elmanet.info/). Initially, the data obtained by COMSOL are exported to MATLAB for the calculation of the average flow and focal area. The average flux is obtained by analyzing all the nodes of the receiver surface, and nonzero flux values are identified. The calculation of the focal area is carried out by storing the coordinates furthest from the focal point that has recorded a flux value other than zero. The x and y coordinates obtained represent the semiaxes of an ellipse and the focal area can be calculated as follows:

$$A_{\text{FOC}} = \pi \cdot x \cdot y. \quad (1)$$

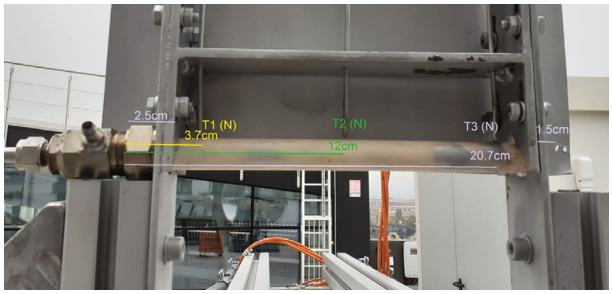

Figure 3: Focal plane and position of N-type thermocouples.

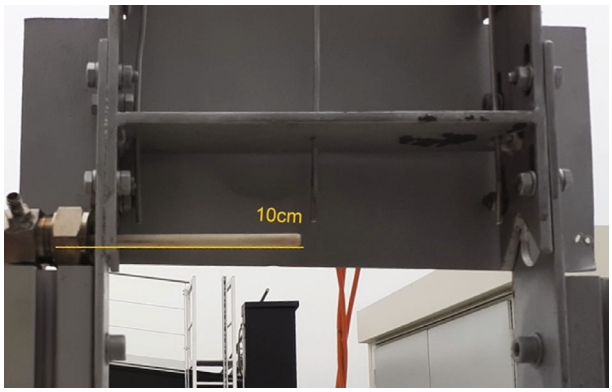

Figure 4: Thermocouple T0 (type B) inside the receiver (same position of T2 thermocouple).

The incident power on the receiver is obtained as follows:

$$Q_{\text{ott}} = \Phi_{\text{ave}} \cdot A_{\text{FOC}}. \tag{2}$$

Once the receiver power has been obtained, it is necessary to calculate the power deposited by the concentrator.

$$Q_C = A_C \cdot G, \tag{3}$$

where A_C represents the area of the concentrator and G is the direct normal irradiation. It is now possible to derive the optical efficiency (η_{ott}) of the paraboloid (see Table 4).

$$\eta_{\text{ott}} = \frac{Q_{\text{ott}}}{Q_C}. \tag{4}$$

Table 4 shows the parameters resulting from the optical model; the optical efficiency is calculated.

The optical efficiency of the concentrator (η_{ott}), as stated by the manufacturer, can reach a value of 80% when the direct solar irradiation (G) is equal to 800 W/m^2 [32]. The optical model does not consider the thermal dispersion losses of the receiver due to convection and radiation. Another model is created to account for these losses as well.

3.2. Choosing the Appropriate Mesh. Once the optical simulation is completed, the accuracy and reliability of the results obtained must be verified. These parameters directly depend on the type of discretization performed. To clarify the extent of the error made by choosing a less dense mesh type, the one adopted in the optical simulation ("Extremely Fine") is taken as a reference. The relative error is calculated concerning a value obtained from the reference mesh, and considerations are made. By exporting the maximum temperature and maximum flux values in real conditions for each mesh, the following graph is obtained (see Figure 10).

The figure shows the relative error committed when calculating the maximum flux incident on the receiver and the maximum temperature. The error on the maximum temperature does not exceed 10% regardless of the choice of mesh adopted, following the appropriate spacing interval (dx). It should also be considered that an error of just over 5% can cause a temperature difference of over 550 K compared to the case of a denser mesh. A different error can be made for the maximum flow which, in less dense mesh configurations, has an error of over 20% (see Table 5). A larger error occurs because the order of magnitude of the maximum flow is 10^7-10^6 W/m^2, and the computational calculation suffers when the number to be obtained is described by many digits.

From Table 5, the most advantageous spatial discretization is the first three conditions (A, B, and C); the first two can be used indiscriminately as they have the same values (A and B). To lighten the calculation, the second discretization (B) is more advantageous than the first (A).

3.3. Thermal Model. Thermal losses must also be included to approximate the model to real conditions. Thermal losses can be divided into the following:

(i) Convective losses

(ii) Radiative losses

The former occurs due to a temperature difference between the outside air and the surface temperature of the receiver. Convective air motions generate heat losses, which results in a reduction of the working fluid flow rate and a reduction of the maximum temperature.

$$Q_{\text{conv}} = h \cdot A_R \cdot \Delta T. \tag{5}$$

The radiative losses are due to the surface of the receiver, which radiates heat outside following the Stefan-Boltzmann law.

$$Q_{\text{rad}} = \varepsilon \cdot \sigma \cdot A_R \cdot \left(T_{\text{amb}}^4 - T_R^4\right). \tag{6}$$

The radiative losses depend on the emission at the surface temperature of the receiver (T_R). The model was created using the module "heat transfer in solids," which allows to study the behavior of materials in steady or transient conditions. To simplify the discussion, only the steady state will be taken into account. Two cases are analyzed for the model:

(i) Optimal Case: The convective losses assuming laminar convection and neglecting the radiation losses

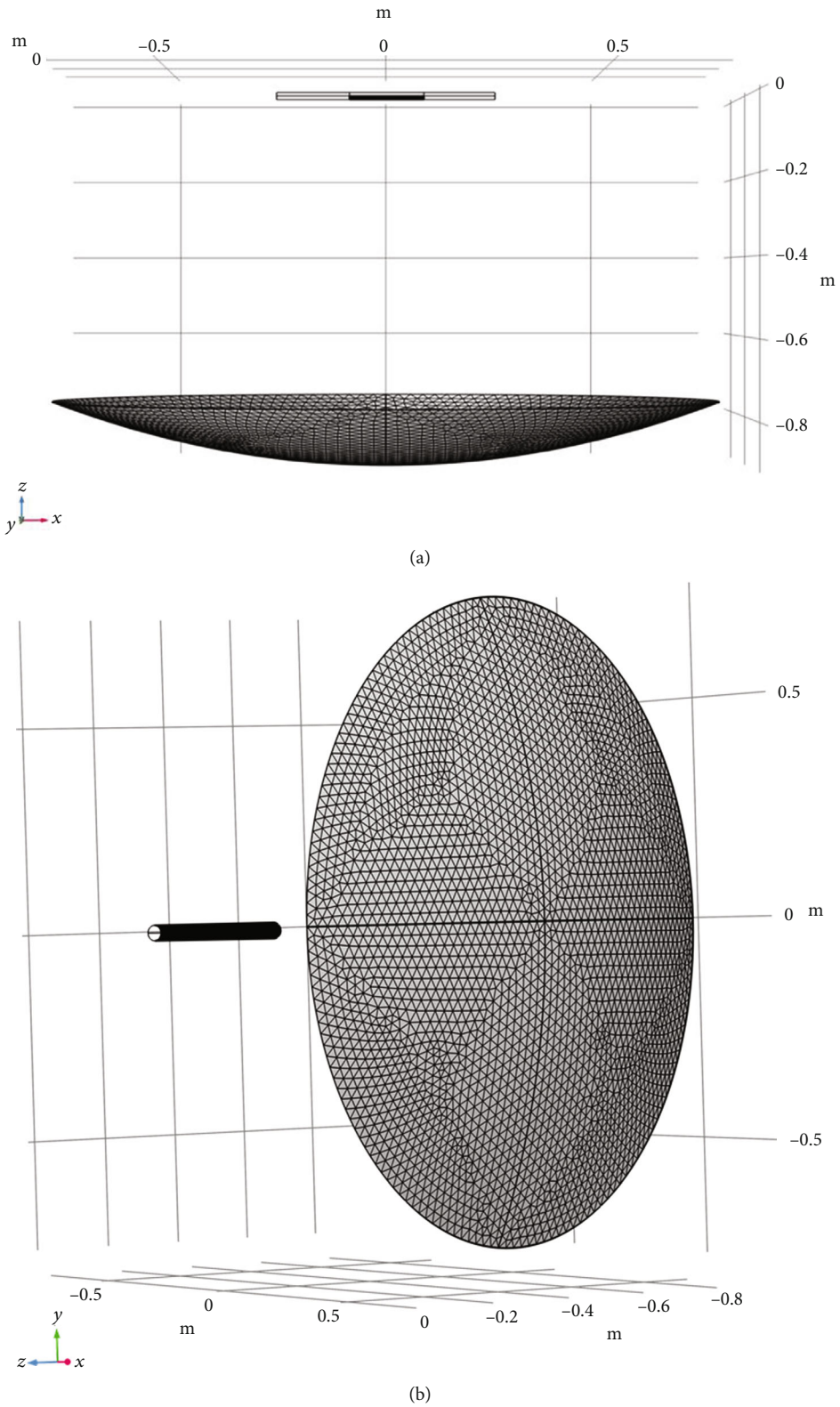

Figure 5: Mesh CSP configuration: "Extremely Fine"—(a) view 1 (top view) and (b) view 2 (side view).

Figure 6: Focus on mesh for the receiver.

(ii) Real Case: The convection will be of the forced type, and the radiation losses will be considered

3.3.1. Ideal Case of the Optical Model. The 2D modelling considers the diameter of the receiver and length as the distance between the two thermocouples (T1 and T3). Assuming a focal radius of 5 mm has been assumed and the heat transfer coefficient (h) under laminar conditions, Figure 11 is obtained.

In the optimal case, the maximum temperature reached is 1819°C; the manufacturer's manual states that in the optimal conditions, the reflector can converge with the rays obtaining temperatures higher than 1800°C. The input conditions to obtain the result are summarized as follows:

(i) The receiver material is made of 99.7% sintered alumina (Al_2O_3) with thermal conductivity $k = 38.5\ W/(m^2 \cdot K)$ [34]

(ii) The average incident flux used in the optical model from MATLAB simulation ($\Phi_{ave} = 2.28 \cdot 10^6\ W/m^2$)

(iii) The heat transfer coefficient (h) was calculated under laminar conditions

(iv) The ambient conditions were considered at $T_{amb} = 20°C$ and $p_{amb} = 1$ atm

The heat transfer coefficient (h) was obtained considering the following experimental equation:

$$h = \frac{k}{D} \cdot \left(0.6 + \frac{0.387 Ra_D^{1/6}}{\left(1 + (0.559/\mathrm{Pr})^{9/16}\right)^{8/27}} \right)^2. \quad (7)$$

The Prandtl (Pr) and Rayleigh (Ra) numbers of air were evaluated at atmospheric pressure and at the average between the ambient temperature (T_{amb}) and the average temperature of the receiver ($\bar{T}_R$) using the REFPROP software (NIST, USA).

3.3.2. Real Case of the Optical Model. To evaluate the thermal properties of the receiver and validate the experimental model, it is good to consider all the loss contributions at the worst real conditions. In this case, the radiation losses and convective losses will be added to an exchange coefficient calculated in turbulent conditions. Assuming a focal radius of 8 mm, Figure 12 is obtained.

Unlike the optimal case, lower temperatures are reached due to forced convection. The extremities, further away from the source, also have a significantly lower temperature gradient.

The environmental, flow, and material input conditions remain unchanged. Compared to the optimal case, the differences are as follows:

(i) Coefficient h calculated in forced convection, assuming a wind speed of $u = 1.2$ m/s

(ii) Radiative losses obtained assuming an emissivity of $\varepsilon = 0.4$ [35]

The heat transfer coefficient was obtained considering the following experimental equation:

$$h = \frac{k}{D} \left(0.3 + \frac{0.62 Re_D^{1/2} \cdot \mathrm{Pr}^{1/3}}{\left(1 + (0.4/\mathrm{Pr})^{2/3}\right)^{1/4}} \cdot \left(1 + \left(\frac{Re_D}{282000} \right)^{5/8} \right)^{4/5} \right) \quad (8)$$

The calculation of the coefficient h depends on the Prandtl number and the Reynolds number, which in turn is directly proportional to the wind speed. The decrease in the maximum temperature depends on the wind, which favours the increase in convection losses. The thermal losses are evaluated, calculating the contributions of radiation and convection analytically. Initially, the average temperature of the receiver ($\bar{T}_R$) is obtained from the mapping obtained on COMSOL, then the properties of the air are evaluated by averaging between $\bar{T}_R$ and T_{amb}. Once the properties of the air have been obtained from REFPROP, the coefficient h is estimated to derive the convective losses; the radiative ones are calculated assuming an emissivity of 0.4 [35]. For the calculation of the liminal exchange coefficient, reference is made to relation 7, and the convective and radiative losses are calculated, respectively, from Equations (5) and (6). Now, it is possible to obtain thermal efficiency through the following relation:

$$\eta_{th} = \frac{Q_{UT}}{Q_{ott}} = \frac{Q_{ott} - Q_{conv} - Q_{rad}}{Q_{ott}}. \quad (9)$$

Table 6 shows the parameters resulting from the thermal model, in the real case. The power output without optical losses (Q_{ott}) is deducted from convection-related (Q_{conv}) and radiative (Q_{rad}) losses. This results in the incident power output and the resulting average temperature recorded at the receiver ($\overline{T_R}$).

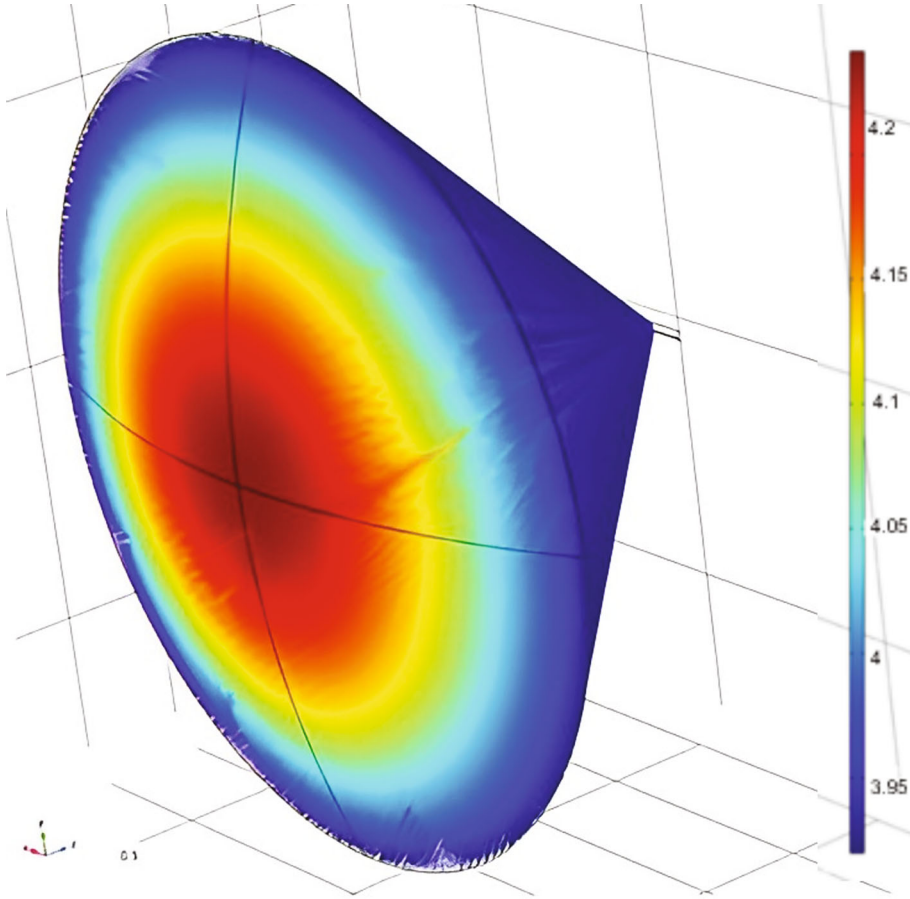

(a) Ideal case

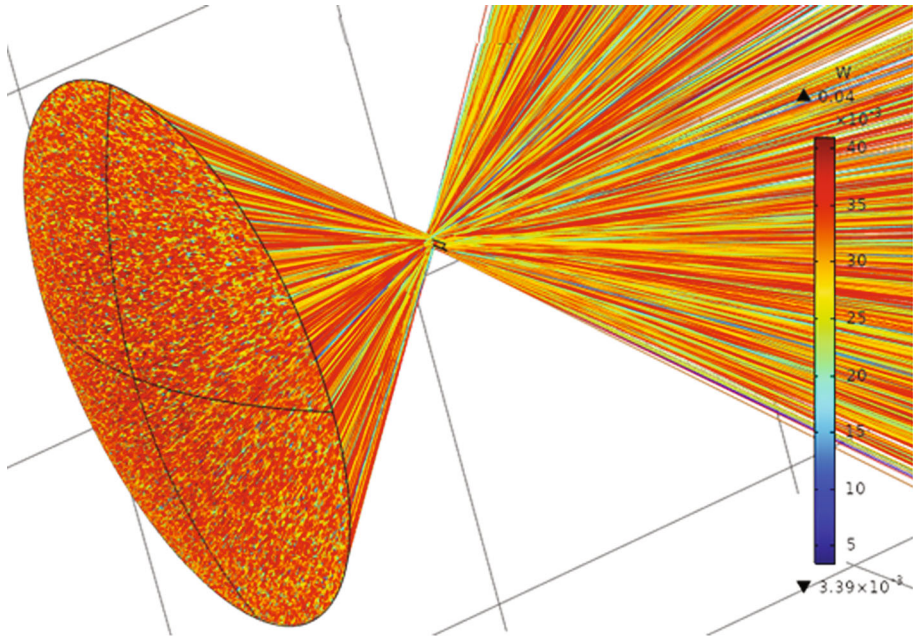

(b) Real case

FIGURE 7: Monte Carlo ray tracing simulation concentrated on the receiver (ideal case—3.95 to $4.2 \cdot 10^{-2}$ (a) vs. real case—3.4 to $40 \cdot 10^{-3}$ (b)).

Table 2: Input data optical model.

Name	Value	Description
G	800 W/m^2	Direct normal irradiation
n_{rays}	10^5	Number of rays
α_r	0.2	Absorption coefficient of the reflector
θ_s	4.65 mrad	Sun-earth angle

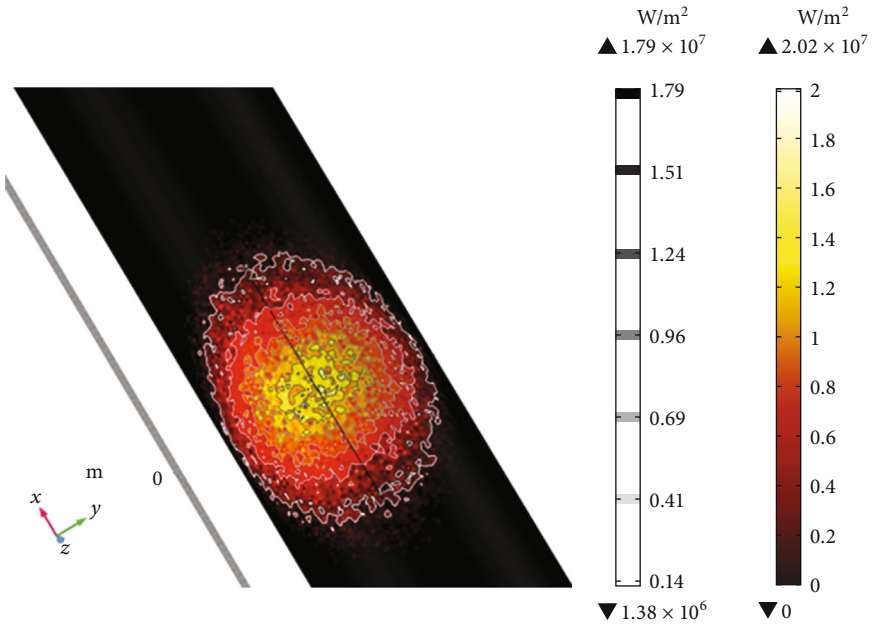

(a) Ideal case

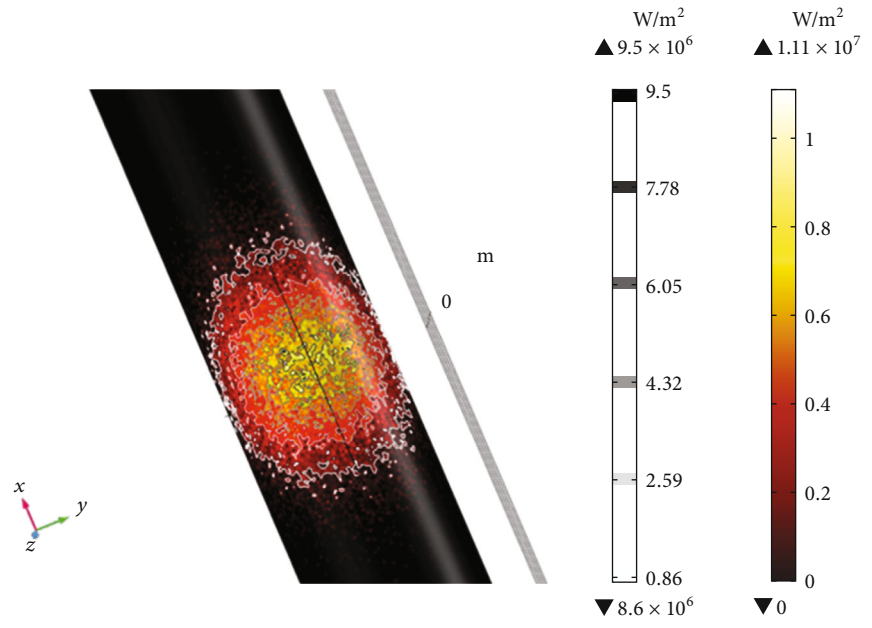

(b) Real case

Figure 8: Receiver heat flow distribution (ideal case (a) vs. real case (b)).

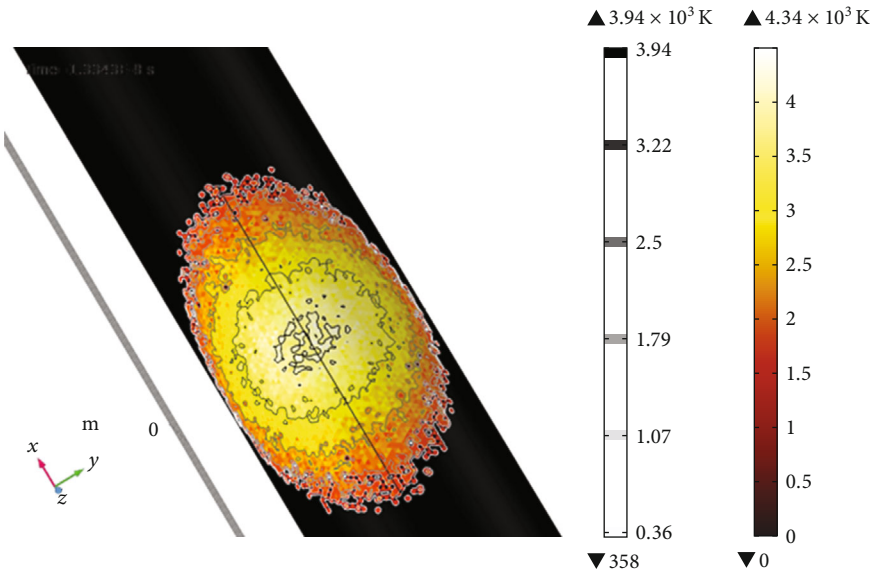

(a) Ideal case

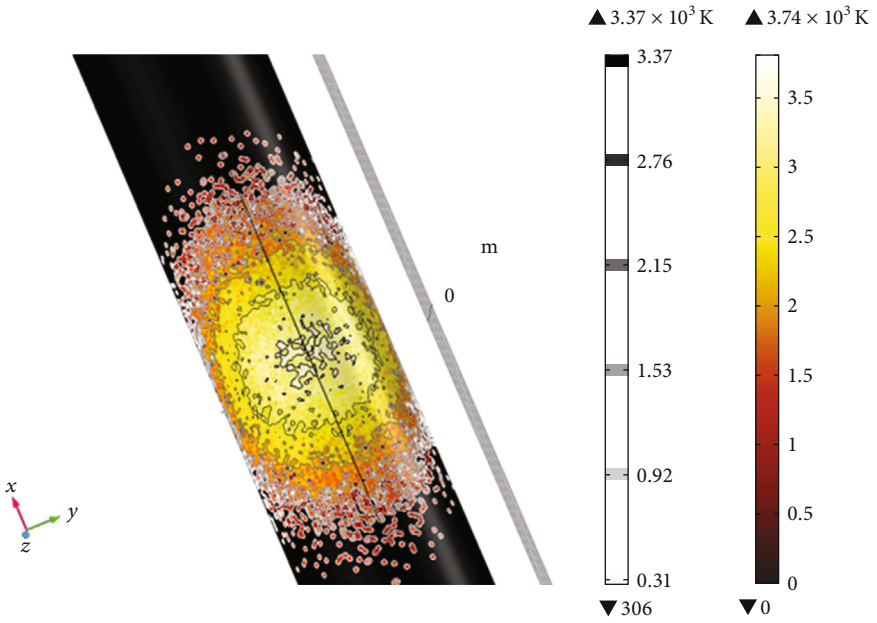

(b) Real case

Figure 9: Receiver temperature distribution (ideal case vs. real case).

Table 3: Output value optic simulation.

Case	Φ_{max}	T_{max}
Ideal	$2.02 \cdot 10^7$ W/m^2	4344 K
Real	$1.11 \cdot 10^7$ W/m^2	3739 K

The total efficiency of the CSP can be estimated as follows:

$$\eta_{UT} = \frac{Q_{UT}}{Q_C} = \eta_{ott} \cdot \eta_{th} = 0.77 \cdot 0.79 = 0.61. \quad (10)$$

3.4. Model Validation. To verify the validity of the model created, it must be compared with the data recorded by the thermocouples. Three days of the year with no precipitation are taken as a reference to maximize the temperature value obtained. The first two days will have the same configuration as the thermocouples; however, the last will have a different configuration. The data taken from a specific point of the receiver will be compared, which should correspond to the positioning of the thermocouple T0. To lighten the computational calculation, the quantities will be analyzed at an interval of half an hour. Since both the optical and thermal models were created considering the system in stationary conditions, before selecting the time slot, the thermocouple

Table 4: Optical performance and focal area.

Φ_{ave} (W/m^2)	x (m)	y (m)	A_{FOC} (m^2)	Q_{ott} (kW)	Q_C (kW)	η_{ott} (-)
$2.28 \cdot 10^6$	$2.43 \cdot 10^{-2}$	0.009	$6.87 \cdot 10^{-4}$	1.567	2.035	0.77

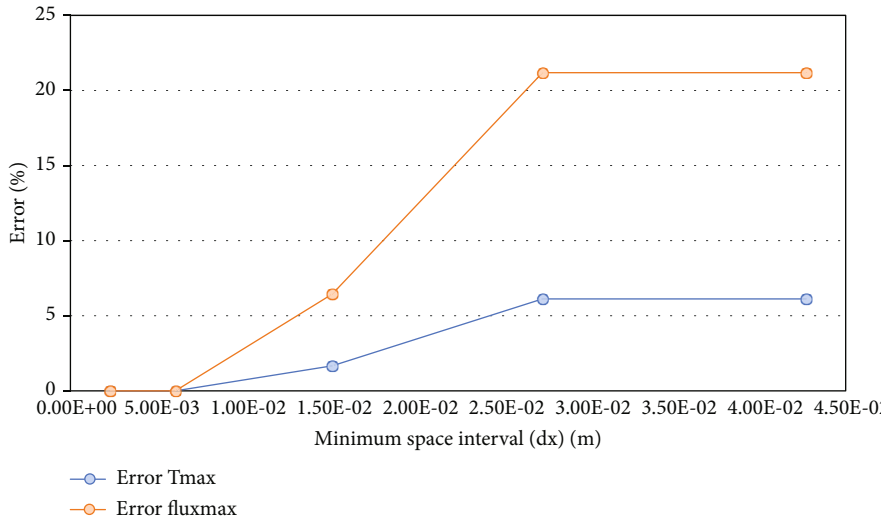

Figure 10: Mesh selection for the independence analysis.

Table 5: Mesh independence analysis—summary table.

Case	dx (m)	Φ_{max} (W/m^2)	T_{max} (K)	$Err_{T_{max}}$ (%)	$Err_{\varphi_{max}}$ (%)
A	$2.29 \cdot 10^{-03}$	$1.11 \cdot 10^{+07}$	3739	0.0	0.0
B	$6.10 \cdot 10^{-03}$	$1.11 \cdot 10^{+07}$	3739	0.0	0.0
C	$1.52 \cdot 10^{-02}$	$1.04 \cdot 10^{+07}$	3676.9	1.7	6.5
D	$2.74 \cdot 10^{-02}$	$8.73 \cdot 10^{+06}$	3509.5	6.1	21.2
E	$4.27 \cdot 10^{-02}$	$8.73 \cdot 10^{+06}$	3509.5	6.1	21.2

trend will be studied, avoiding sudden changes in the temperature recording. On the roof of the Energy Center (Turin, Italy), there is a weather station, which records the environmental conditions every quarter of an hour for every day of the year including solar irradiance, wind speed, and outside temperature.

The procedure adopted for each day is summarized as follows:

(1) In the optical performance model, the flows incident on the receiver are calculated by taking as reference the irradiance values recorded by the weather station

(2) The average incident flows for the various cases are calculated from the MATLAB code

(3) The thermal model is implemented by inserting as input data the average flow, the wind speed, and the external temperature obtained from the weather station

(4) The temperature data of the receiver are exported from the thermal model in correspondence with the thermocouple T0

(5) The data obtained from the model is compared with the data recorded by the B thermocouple

3.4.1. 17 January 2020. The temperature trend recorded by the thermocouple T0 is reported below for day 1 (17/01/2020), (see Figure 13).

The experimental model created on COMSOL does not consider the transient phenomenon, so the charging and discharging phases will be excluded from the discussion. Once the time slot of interest has been chosen (between 1:30 pm and 3:30 pm, CET), the procedure described previously is followed. The temperature point exported from the model at the position of the thermocouple T0 is visible in Figure 14.

Now, it is possible to generate a graph that compares the temperatures measured by the thermocouple with those obtained from the model (see Figure 15).

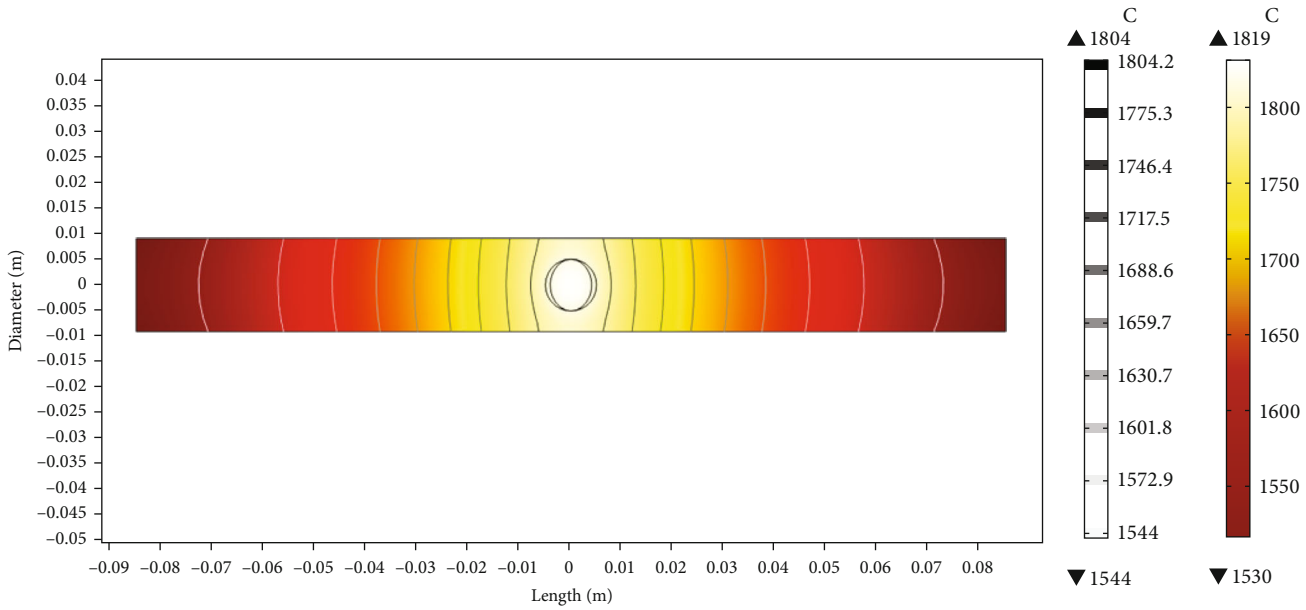

Figure 11: Thermal model, ideal case—temperature distribution of the receiver, cylindrical shape, and longitudinal view.

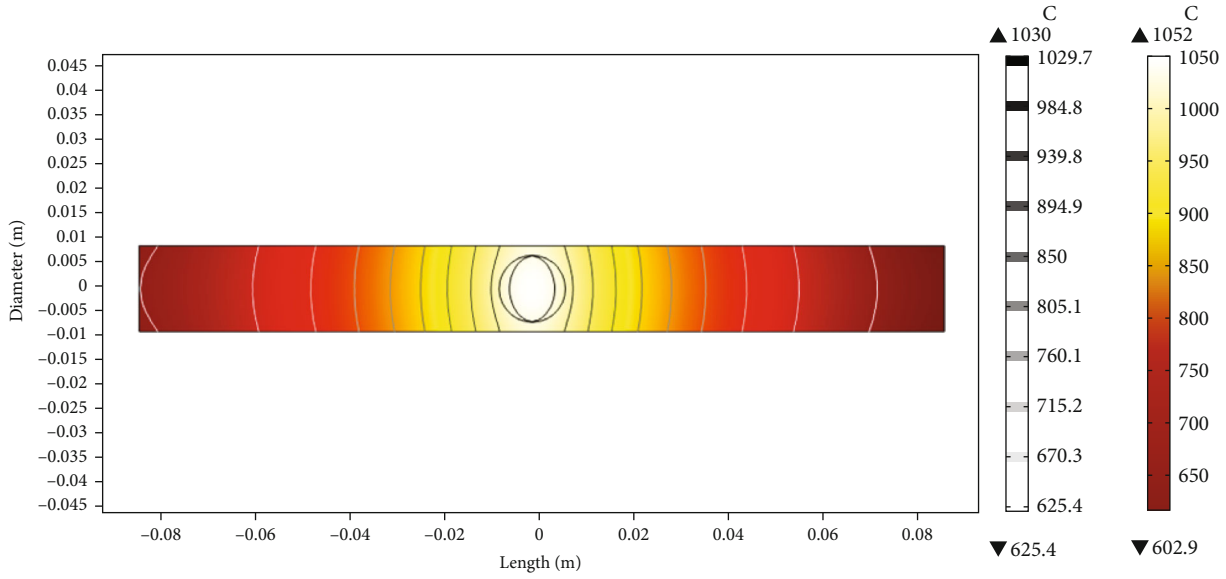

Figure 12: Thermal model, real case—temperature distribution of the receiver, cylindrical shape, and longitudinal view.

Table 6: Thermal losses and thermal efficiency.

$\bar{T}_R$ (K)	Q_{ott} (W)	Q_{conv} (W)	Q_{rad} (W)	η_{th} (-)
1091	1567	68.14	104.59	0.79

The last two values have the largest point error, which is due to the transient phenomenon: the receiver, at high temperatures, slowly reduces its temperature compared to the model which performs an instant-by-instant analysis.

3.4.2. 10 March 2020. The temperature trend recorded by the thermocouple T0 is reported below for day 2 (10/03/2020), (see Figure 16).

The temperature trend does not show sudden changes in March; for this reason, it was decided to compare the model temperatures in the same time interval as in January (see Figure 17).

The experimental model varies greatly depending on the amount of direct normal irradiation (G) which invests the paraboloid. The highest experimental temperature is recorded when the irradiance is higher (at 2 pm, CET). The model

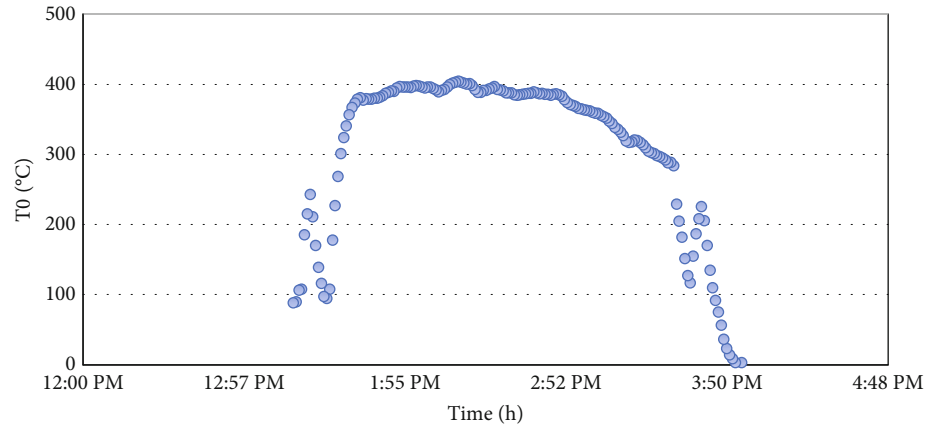

Figure 13: Evaluation of the temperature collected by the T0 sensor versus time, for January 17, 2020. They are recorded from 12 h noon to 4:48 h in the afternoon.

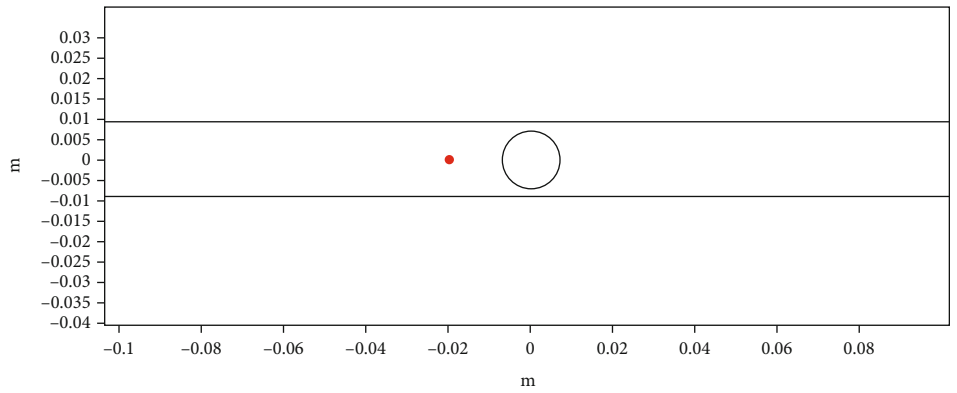

Figure 14: Longitudinal receiver view and T0 thermocouple position (red point)—Comsol model.

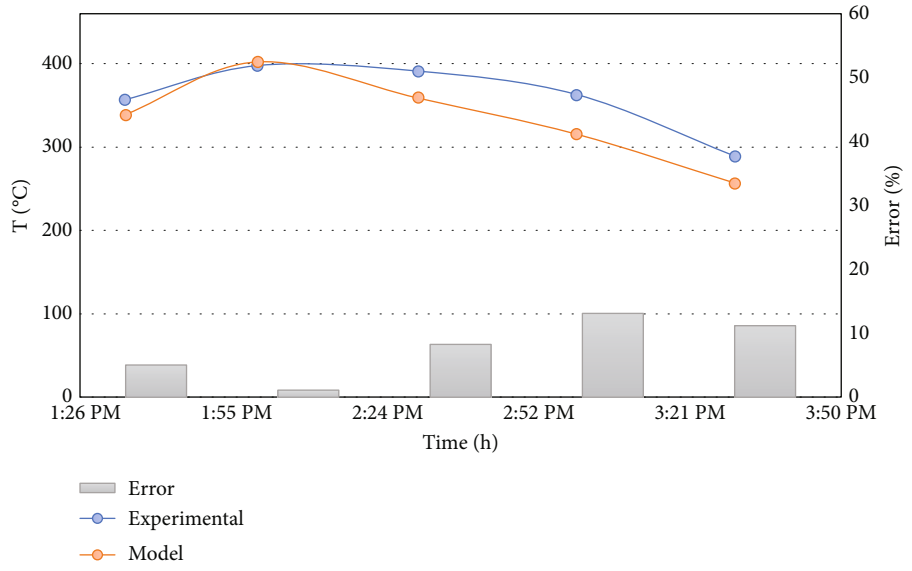

Figure 15: Comparison data between thermocouple T0 and output model—17/01/2020.

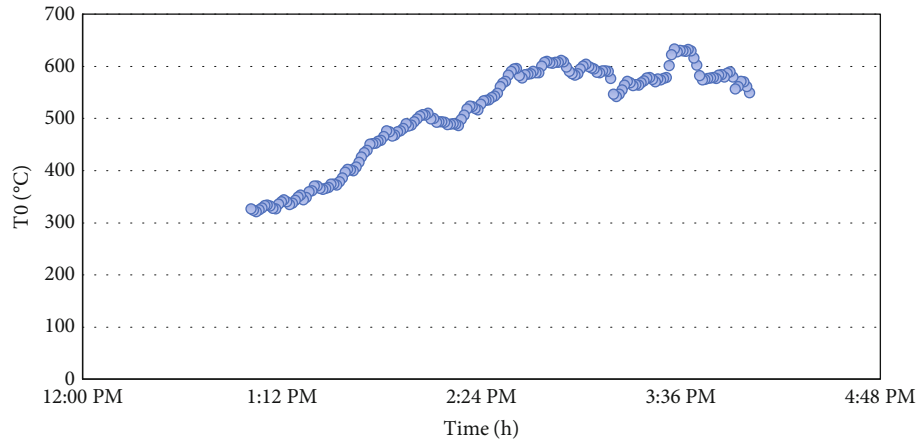

Figure 16: Evaluation of the temperature collected by the T0 sensor versus time, for March 10, 2020. They are recorded from 12 h noon to 4:48 h in the afternoon.

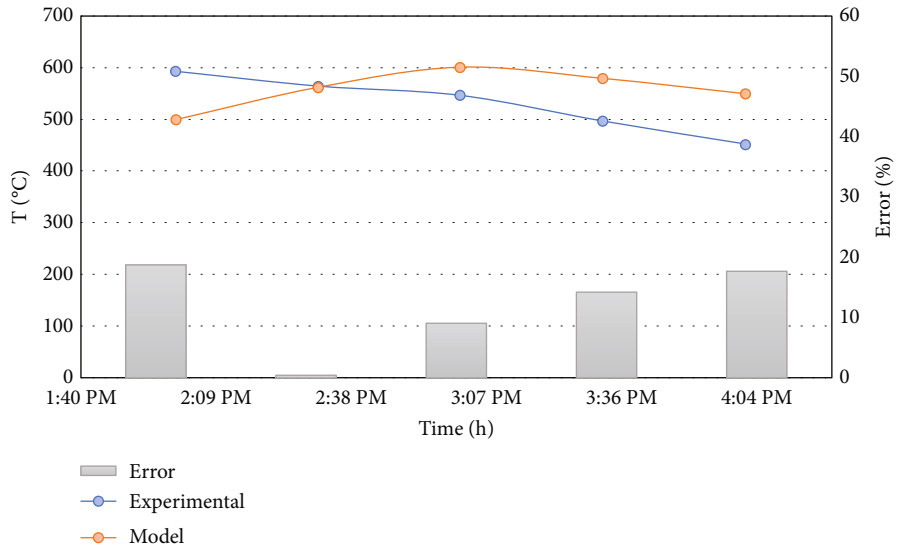

Figure 17: Comparison data between thermocouple T0 and output model—10/03/2020.

Table 7: Average error between the model and the experimental average value of temperature.

	T0 average (experimental) (°C)	T average (model) (°C)	Error (%)
17/01/2020	359.5	334.3	7.0
10/03/2020	532.3	542.6	1.9

temperature shows the maximum temperature value at 3 pm, CET due to the transient phenomena of the material, which accumulates the heat received in the previous hours. Despite the point error approaching 20%, the temperature trend in the time interval considered is almost similar. The average value of the temperatures is calculated in the two intervals.

The last column of Table 7 shows the deviation (Error (%)) between the mean temperature value obtained from the model and the experimentally measured value.

The average error is acceptable; the model describes the real temperature trend and can be used for system dimensioning. Finally, the model can be used to assess the seasonal average trend of the maximum temperature at the receiver on a typical day.

One of the fundamental parameters for the development of temperature trends is direct solar irradiance. To assess the seasonal trend in irradiance, averages were obtained between the values corresponding to the central day of each month, in the case of a clear, sunny day. These data are recorded experimentally. Otherwise, the days adjacent to or following the central day were taken as references; these data are reported in Figure 18.

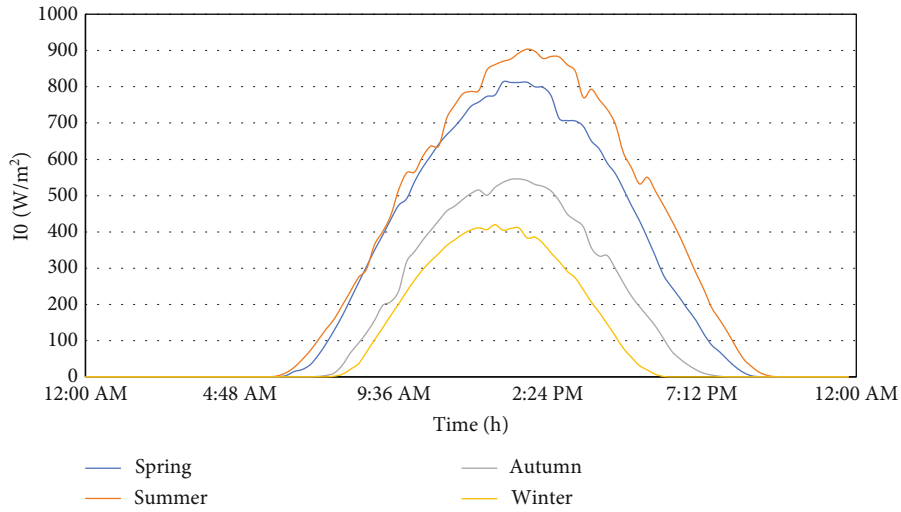

Figure 18: Average daily irradiance per season (year 2019).

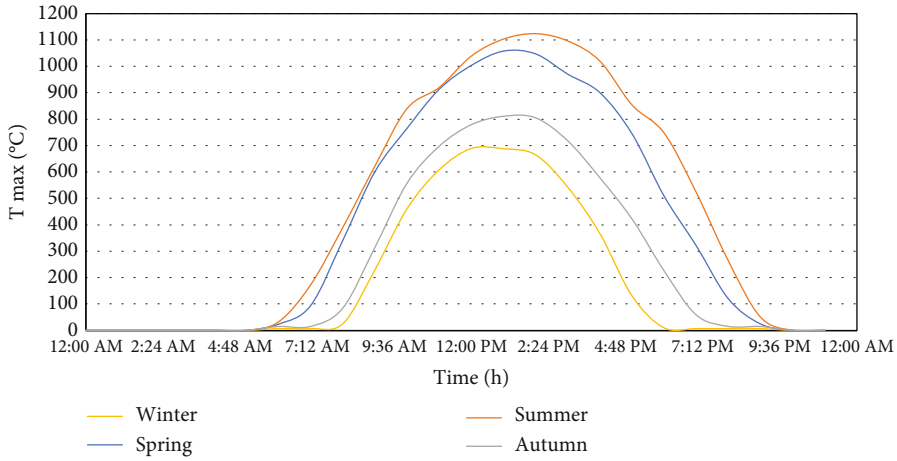

Figure 19: Maximum seasonal average receiver temperature. The temperature obtained at the extremes does not coincide with zero but tends to the ambient temperature (zero taken as reference T_{amb}) (year 2019).

The summer season has the highest values of global radiation and a wider curve during the day, allowing to increase in the plant's producibility when compared to other seasons. The peak values, for all seasons, are recorded between 1 pm and 2 pm CET. Following the same procedure adopted in the validation of the experimental model, the seasonal temperature trend in the receiver is obtained (see Figure 19).

The maximum temperature reached by the receiver is approximately 1124°C. To simplify the computational calculation of the model, the data were processed hour by hour, and the other environmental conditions to be included in the thermal model were obtained by averaging the wind speed and outside temperature daily. However, in a future article, the data obtained will be taken as a reference and used as input to power a small organic Rankine cycle (10 electrical kW).

4. Conclusions

The findings of this investigation have significant implications for the small electrical power system driven by solar energy. The main contributions of the model can be generalized and summarized as follows:

(1) To take an existing CSP plant as a reference and report its physical and material characteristics as input for the simulation

(2) For the optical simulation, it is preferable to consider the real case on COMSOL, which maintains a heterogeneous distribution of solar energy and a larger portion of sunlight on the reflector that generates a lower temperature and flux than the ideal case

(3) Before proceeding with the thermal model, it is preferable to evaluate the mesh independence analysis

(4) For the thermal simulation, the worst conditions are considered under turbulent conditions, also evaluating the effect of wind speed. Within 2 m/s, the maximum temperature in the receiver exceeds 1000°C, while when there is almost no wind, values close to

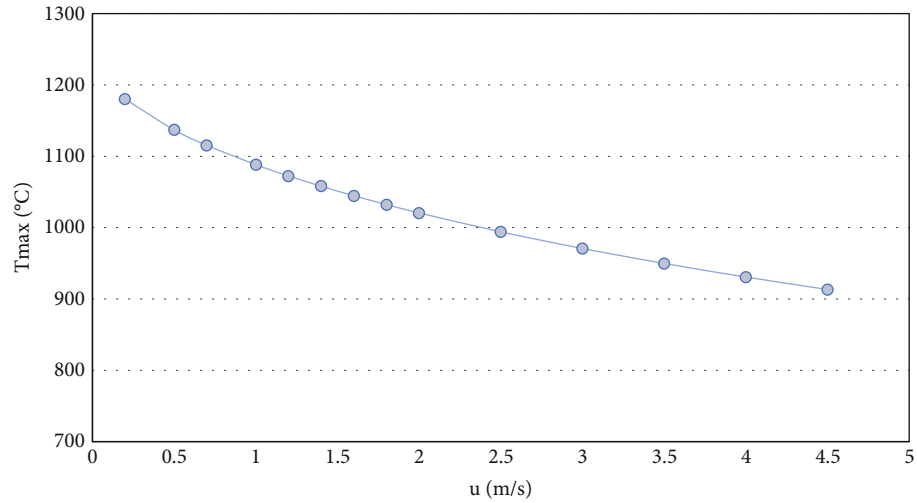

Figure 20: Maximum receiver temperature based on wind speed.

1200°C can be reached. In the most likely wind conditions in Turin (Italy), between 0 and 2 m/s, the temperature variation in the receiver is roughly around 200°C, see Figure 20

(5) To validate the obtained model, the model output data must be compared with the actual data measured by the thermocouples, and the uncertainty can be calculated. If the error of the obtained data is below the threshold value, the output data can be used as input to size the power cycle

A further study could assess the long-term effects of the validity of the model proposed with experimental data collected over different years.

Nomenclature

CFD: Computational fluid dynamics
CSP: Concentrated solar plant
FEM: Finite element method
LFR: Linear Fresnel reflector
MC: Monte Carlo
ORC: Organic Rankine cycle
PTC: Parabolic trough collector
PV: Photovoltaic
PV-TE: Photovoltaic-thermoeletric
SPD: Solar parabolic dish
SPT: Solar power tower
TES: Thermal energy storage.

Symbols

α_r: Absorption coefficient of the reflector (-)
A_C: Concentrator area (m^2)
A_{FOC}: Focal area (m^2)
A_R: Receiver area (m^2)
dx: Minimum space interval of the mesh (m)
D_C: Concentrator diameter (m)
Q_C: Power absorbed by concentrator (kW)
Q_{ott}: Power without optical losses (Incident power) (kW)
Q_R: Power absorbed by receiver (kW)
Q_{cond}: Conduction losses (W)
Q_{conv}: Convective losses (W)
Q_{rad}: Radiative losses (kW)
R_C: Radius of the concentrator (m)
T_C: Concentrator temperature (K)
T_R: Receiver temperature (K)
$\bar{T}_R$: Receiver average temperature (K)
T_{amb}: Ambient temperature (K)
n_{rays}: Number of rays (-)
Φ_{ave}: Average flux (W/m^2)
Φ_{rim}: Rim angle (rad)
η_{opt}: Optical efficiency (-)
η_{th}: Thermal efficiency (-)
η_{ut}: Total efficiency (-)
θ_s: Sun–earth angle (rad)
C: Concentration ratio (-)
D: Diameter receiver diameter (m)
G: Direct solar coefficient normal irradiation (W/m^2)
Nu: Nusselt number (-)
P: Pressure (bar)
Pr: Prandtl number (-)
Ra: Rayleigh number (-)
Re: Reynold number (-)
f: Focal length (m)
h: Convective coefficient ($W/m^2/K$)
k: Conduction coefficient (W/m/K)
u: Wind velocity (m/s)
x: Vertical semiaxis (m)
y: Horizontal semiaxis (m)
ΔT: Delta temperature (K)
ε: Emission coefficient (-)
μ: Viscosity (Pa·s)
ρ: Density (kg/m^3)
σ: Boltzmann constant ($W/m^2/K^4$).

Data Availability

The data is available upon request by the authors.

Disclosure

This work stems from the study conducted by Antonio Marra during his master's thesis entitled: "Ciclo Rankine organico (ORC) su piccola scala guidato da un concentratore solare (CSP)" supervised by Prof. Papurello.

Conflicts of Interest

The authors declare that they have no conflicts of interest.

References

[1] A. Ramos, M. A. Chatzopoulou, J. Freeman, and E. C. N. Markides, "Optimisation of a high-efficiency solar-driven organic Rankine cycle for applications in the built environment," *Applied Energy*, vol. 228, pp. 755–765, 2018.

[2] L. Hernández-Callejo, S. Gallardo-Saavedra, and E. V. Alonso-Gómez, "A review of photovoltaic systems: design, operation and maintenance," *Solar Energy*, vol. 188, pp. 426–440, 2019.

[3] A. G. Fernández, J. Gomez-Vidal, E. Oró, A. Kruizenga, A. Solé, and E. L. F. Cabeza, "Mainstreaming commercial CSP systems: a technology review," *Renewable Energy*, vol. 140, pp. 152–176, 2019.

[4] X. Liu, S. Kent Hoekman, C. Robbins, and E. P. Ross, "Lifecycle climate impacts and economic performance of commercial-scale solar PV systems: a study of PV systems at Nevada's Desert Research Institute (DRI)," *Solar Energy*, vol. 119, pp. 561–572, 2015.

[5] L. Borghero, M. Bressan, D. Ferrero, M. Santarelli, and E. D. Papurello, "Methane-assisted iron oxides chemical looping in a solar concentrator: a real case study," *Catalysts*, vol. 12, no. 11, p. 11, 2022.

[6] D. Papurello, D. Bertino, and E. M. Santarelli, "CFD performance analysis of a dish-Stirling system for microgeneration," *Processes*, vol. 9, no. 7, p. 1142, 2021.

[7] E. Montà, M. Santarelli, and E. D. Papurello, "Synthetic-gas production through chemical looping process with concentrating solar dish: temperature-distribution evaluation," *Processes*, vol. 10, no. 9, p. 1698, 2022.

[8] T. Cui, Y. Xuan, and E. Q. Li, "Design of a novel concentrating photovoltaic–thermoelectric system incorporated with phase change materials," *Energy Conversion and Management*, vol. 112, pp. 49–60, 2016.

[9] Z. Jiang, A. Palacios, X. Lei et al., "Novel key parameter for eutectic nitrates based nanofluids selection for concentrating solar power (CSP) systems," *Applied Energy*, vol. 235, pp. 529–542, 2019.

[10] M. Petrollese, D. Cocco, and E. G. Cau, "Small-scale CSP plant coupled with an ORC system for providing dispatchable power: the Ottana solar facility," *Energy Procedia*, vol. 129, pp. 708–715, 2017.

[11] R. Islam, N. Bhuiyan, and E. M. Ullah, "An overview of concentrated solar power (CSP) technologies and its opportunities in Bangladesh," in *2017 International Conference on Electrical, Computer and Communication Engineering (ECCE)*, pp. 844–849, Cox's Bazar, Bangladesh, 2017.

[12] M. T. Islam, N. Huda, A. B. Abdullah, and E. R. Saidur, "A comprehensive review of state-of-the-art concentrating solar power (CSP) technologies: current status and research trends," *Renewable and Sustainable Energy Reviews*, vol. 91, pp. 987–1018, 2018.

[13] S. A. Kalogirou, "Solar thermal collectors and applications," *Progress in Energy and Combustion science*, vol. 30, no. 3, pp. 231–295, 2004.

[14] The World Bank, *Concentrating solar power - clean power on demand 24/7*, World Bank, Washington, DC, 2021, https://pubdocs.worldbank.org/en/849341611761898393/WorldBank-CSP-Report-Concentrating-Solar-Power-Clean-Power-on-Demand-24-7-FINAL.pdf (consultato 7 settembre 2021).

[15] A. Mohamad, J. Orfi, and E. H. Alansary, "Heat losses from parabolic trough solar collectors," *International Journal of Energy Research*, vol. 38, no. 1, pp. 20–28, 2014.

[16] A. Fernández-García, E. Zarza, L. Valenzuela, and E. M. Pérez, "Parabolic-trough solar collectors and their applications," *Renewable and Sustainable Energy Reviews*, vol. 14, no. 7, pp. 1695–1721, 2010.

[17] T. Crescenzi, *Opportunità di applicazione delle tecnologie solari termodinamiche in Italia*, ENEA, Roma, 2016.

[18] "Concentrating_solar_power_part_1.pdf," Septembre 2021, https://www.dlr.de/tt/Portaldata/41/Resources/dokumente/institut/system/publications/Concentrating_Solar_Power_Part_1.pdf.

[19] A. Ummadisingu and E. M. S. Soni, "Concentrating solar power – technology, potential and policy in India," *Renewable and Sustainable Energy Reviews*, vol. 15, no. 9, pp. 5169–5175, 2011.

[20] M. Z. A. Ab Kadir, Y. Rafeeu, and E. N. M. Adam, "Prospective scenarios for the full solar energy development in Malaysia," *Renewable and Sustainable Energy Reviews*, vol. 14, no. 9, pp. 3023–3031, 2010.

[21] R. Chacartegui, D. Sánchez, J. M. Muñoz, and E. T. Sánchez, "Alternative ORC bottoming cycles FOR combined cycle power plants," *Applied Energy*, vol. 86, no. 10, pp. 2162–2170, 2009.

[22] H. Yu, H. Helland, X. Yu, T. Gundersen, and E. G. Sin, "Optimal design and operation of an organic Rankine cycle (ORC) system driven by solar energy with sensible thermal energy storage," *Energy Conversion and Management*, vol. 244, article 114494, 2021.

[23] A. Boretti, "α-Stirling hydrogen engines for concentrated solar power," *International Journal of Hydrogen Energy*, vol. 46, no. 29, pp. 16241–16247, 2021.

[24] Z. Kazimierski and E. J. Wojewoda, "Comparison of the externally heated air valve engine and the helium Stirling engine," *Energy Conversion and Management*, vol. 80, pp. 357–362, 2014.

[25] P. Danieli, S. Rech, and E. A. Lazzaretto, "Supercritical CO2 and air Brayton-Joule versus ORC systems for heat recovery from glass furnaces: performance and economic evaluation," *Energy*, vol. 168, pp. 295–309, 2019.

[26] J. Coventry and E. C. Andraka, "Dish systems for CSP," *Solar Energy*, vol. 152, pp. 140–170, 2017.

[27] A. Fritsch, R. Uhlig, L. Marocco, C. Frantz, R. Flesch, and E. B. Hoffschmidt, "A comparison between transient CFD and FEM simulations of solar central receiver tubes using molten salt and liquid metals," *Solar Energy*, vol. 155, pp. 259–266, 2017.

[28] J. Fang, C. Zhang, N. Tu, J. Wei, and E. Z. Wan, "Thermal characteristics and thermal stress analysis of a superheated water/steam solar cavity receiver under non-uniform concentrated solar irradiation," *Applied Thermal Engineering*, vol. 183, article 116234, 2021.

[29] G. Pierucci, S. Hosouli, M. Salvestroni et al., "Experimental methodology and thermal loss tests on small size absorber

tubes for solar applications," *Energies*, vol. 11, no. 10, p. 2552, 2018.

[30] A. Gilioli et al., "Finite element modelling of a parabolic trough collector for concentrated solar power," *Energies*, vol. 14, no. 1, p. 1, 2021.

[31] "How to model solar concentrators with the ray optics module, COMSOL Multiphysics," https://www.comsol.com/blogs/how-to-model-solar-concentrators-with-the-ray-optics-module/ (consultato 24 agosto 2021).

[32] Manuale uso e manutenzione Concentratore solare a disco El.Ma. srl eletronics.pdf..

[33] "TERSID (Milano)-Termocoppie.pdf," Giugno 2021. https://www.tersid.it/files/documentoprodotto/2020/2_termocoppie_kXMVjwz.pdf.

[34] "Properties: alumina - aluminium oxide - Al2O3 - a refractory ceramic oxide, AZoM.com," https://www.azom.com/properties.aspx?ArticleID =52 (consultato 1 settembre 2021).

[35] "Black body calculations," http://lenr.qumbu.com/blackbody_141027A.php (consultato 17 maggio 2021).